Original article

Development of dynamic motion models of SPACE code for ocean nuclear reactor analysis

Byoung Jae Kim [a], *, Seung Wook Lee [b]

[a] School of Mechanical Engineering, Chungnam National University, 99 Daehak-ro, Yuseong-gu, Daejeon, 34134, Republic of Korea
[b] Virtual Nuclear Power Plant Technology Development Division, Korea Atomic Energy Research Institute, 111, Daedeock-daero 989, Yuseong-gu, Daejeon, 34057, Republic of Korea

A B S T R A C T

Lately, ocean nuclear power plants have attracted attention as one of diverse uses of nuclear power plants. Because ocean nuclear power plants are movable or transportable, it is necessary to analyze the thermal hydraulics in a moving frame of reference, and computer codes have been developed to predict thermal hydraulics in large moving systems. The purpose of this study is to incorporate a three dimensional dynamic motion model into the SPACE code (Safety and Performance Analysis CodE) so that the code is able to analyze thermal hydraulics in an ocean nuclear power plant. A rotation system that describes three-dimensional rotations about an arbitrary axis was implemented, and modifications were made to the one-dimensional momentum equations to reflect the rectilinear and rotational acceleration effects. To demonstrate the code's ability to solve a problem utilizing a rotational frame of reference, code calculations were conducted on various conceptual problems in the two-dimensional and three-dimensional pipeline loops. In particular, the code results for the three-dimensional pipeline loop with a tilted rotation axis agreed well with the multi-dimensional CFD results.
© 2021 Korean Nuclear Society, Published by Elsevier Korea LLC. This is an open access article under the CC BY-NC-ND license (http://creativecommons.org/licenses/by-nc-nd/4.0/).

1. Introduction

Lately, ocean nuclear power plants have attracted attention as one of diverse uses of nuclear power plants. There are various types of ocean nuclear power plants [1–4], having designs that can be categorized into floating, gravity-based, and submerged categories. Each design has its own advantages and disadvantages [2].

In general, ocean nuclear power plants are movable or transportable. Therefore, it is important to investigate the thermal hydraulics in a moving frame of reference, and various efforts have been made to develop computer code that can be used to predict thermal hydraulics in large moving systems.

In early code development work, the RETRAN code was modified to consider the effect of the motion of an ocean nuclear plant [5–7], which played a pioneering role in the transient analysis of thermal hydraulics in moving systems. The RETRAN code allows a velocity slip using a drift-flux model. In recent code development work, thermal-hydraulics code based on two-fluid models—such as RELAP5 and MARS-KS—were modified to consider the effect of the

dynamic motion of an ocean nuclear power plant [8–10]. More recently, multidimensional two-fluid equations have been systematically formulated [11].

Yan and Yu [10] modified the one-dimensional momentum equations in the RELAP5/MOD3.3 code to consider the rotational acceleration effects such as centrifugal and Euler forces. To validate the developed code, a two-phase natural circulation flow was investigated under rolling conditions. Mesina et al. [9] also modified the one-dimensional momentum equations in the RELAP5-3D code to consider translational and rotational acceleration effects. To demonstrate the ability of the code to solve a problem utilizing a rotational frame of reference, the motion of water in a rolling manometer was investigated. However, the oscillation period was so large that the motion of the water was governed by changes in the direction of gravity rather than the rotational acceleration effects. Beom et al. [8] modified the one-dimensional momentum equations in the MARS-KS code to consider the translational and rotational acceleration effects. The motion of water in a rotating or oscillatory manometer was investigated. Because the rotation speed was low or the oscillation period large, the motion of water was governed by changes in the direction of gravity rather than the rotational acceleration effects.

* Corresponding author.
  E-mail address: bjkim@cnu.ac.kr (B.J. Kim).

Most existing works usually adopted the rotation system based on the intrinsic Tait-Bryan angles. Here, the intrinsic rotation means rotations about the axes of the rotating coordinate system that changes after each elemental rotation. Tait-Bryan angles use different axes for the three elemental rotations (e.g., the first rotation about the x-axis, the second rotation about the y-axis, and the third rotation about the z-axis) [12]. Tait-Bryan angles are also called yaw, pitch, and roll. The intrinsic Tait-Bryan angles may describe the three-dimensional rotations. However, a difficulty arises when dealing with a rotation around an arbitrary axis. It is common practice to specify the rotation vector in the fixed (or inertial) coordinates. However, because the roll, pitch, yaw angles are expressed in the rotating coordinates, a complicated conversion process from the rotation specified in the fixed coordinates into the rotation in the intrinsic Tait-Bryan angles is required. If the rotation axis is parallel to one of axes of the fixed coordinates, the conversion is not necessary and the rotation is actually two-dimensional. The existing works considered only the rotations about one of axes of the fixed coordinates, so their verifications were not general. A simpler rotation system is required to implement the three-dimensional rotation about an arbitrary axis.

Meanwhile, the SPACE code is the latest thermal-hydraulics code developed by the Korean nuclear industry [13]. The hydraulic solver adopts two-fluid and three-field governing equations that comprise gas, continuous liquid, and droplet fields. The purpose of this study is to incorporate a three-dimensional dynamic motion model into the SPACE code so that it can analyze thermal hydraulics in an ocean nuclear power plant. A simpler rotation system that describes three-dimensional rotations about an arbitrary axis was implemented into the code. Various conceptual problems were tested to verify the dynamic motion model for general rotations. In particular, the effects of the centrifugal and Euler forces were also quantitatively examined.

2. Methodology: dynamic motion models

An ocean nuclear reactor may undergo translational and rotational accelerations. Fig. 1 shows a particle (P) of matter in an offshore structure. Three reference frames are used. The first is the inertial (or fixed) reference frame (XYZ) centered at O_I. The unit direction vectors are denoted by **I**, **J**, and **K**, respectively. The second is the non-inertial (or metacenter) reference frame centered at O_M. The power plant is assumed to rotate with an angular velocity **Ω** that has its origin at O_M. The unit direction vectors are denoted by **i**, **j** and **k**, respectively. The third is the relative (or plant) reference frame (x′y′z′) centered at O_R, which moves in tandem with the non-inertial reference frame. The axes of the relative reference frames are oriented for convenient power plant analysis. The unit direction vectors are denoted by **i′**, **j′**, and **k′**, respectively. The position vectors from O_I to O_M, O_M to P, and O_R to O_M are **R**, **r**, and **r̄**, respectively.

Fig. 2 show a one-dimensional hydrodynamic component, such as a cell, in the inertial frame of reference. The direction of the component is expressed using the inclination angle (θ) and the azimuthal angle (φ), in the inertial reference frame. The azimuthal angle is defined as the angle from the X-axis to the projected line of the component onto the horizontal XY plane and has a value between $-\pi$ (clockwise 180°) and π (counterclockwise 180°). The inclination angle is defined as the angle from the horizontal plane to the component and has a value between $-\pi/2$ (downward vertical) and $\pi/2$ (upward vertical). Assume that the hydrodynamic component is rotated about an arbitrary axis in the inertial frame of reference. Let the rotation speed vector be $\mathbf{\Omega} = \Omega_X \mathbf{I} + \Omega_Y \mathbf{J} + \Omega_Z \mathbf{K}$. Then, the rotation axis direction unit vector is given by $(e_X, e_Y, e_Z) = (\Omega_X/|\mathbf{\Omega}|, \Omega_Y/|\mathbf{\Omega}|, \Omega_Z/|\mathbf{\Omega}|)$.

The SPACE code adopted a rotation system based on the rotation matrix **R** by angle α around the rotation axis [14].

$$\mathbf{R} = \begin{bmatrix} \cos\alpha + e_X^2(1-\cos\alpha) & e_X e_Y(1-\cos\alpha) - e_Z\sin\alpha & e_X e_Z(1-\cos\alpha) + e_Y\sin\alpha \\ e_Y e_X(1-\cos\alpha) + e_Z\sin\alpha & \cos\alpha + e_Y^2(1-\cos\alpha) & e_Y e_Z(1-\cos\alpha) - e_X\sin\alpha \\ e_Z e_X(1-\cos\alpha) - e_Y\sin\alpha & e_Z e_Y(1-\cos\alpha) + e_X\sin\alpha & \cos\alpha + e_Z^2(1-\cos\alpha) \end{bmatrix} \tag{1}$$
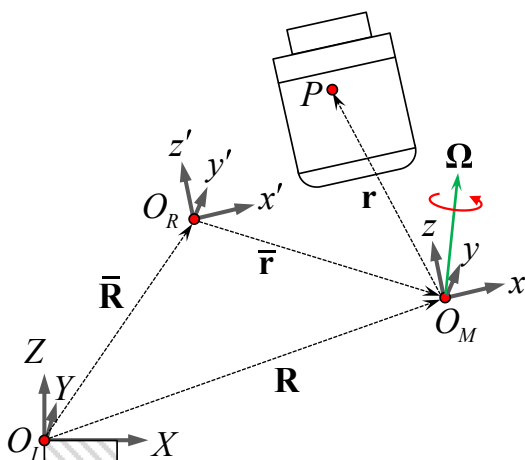

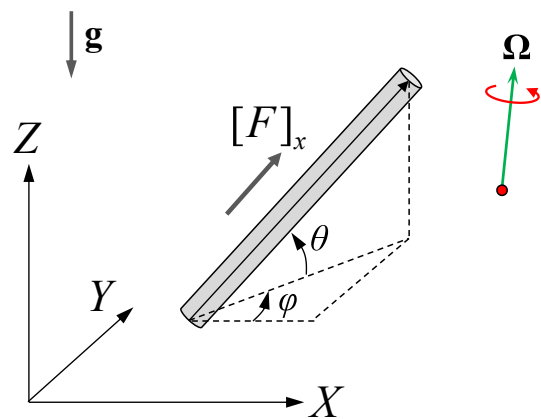**Fig. 1.** Location of a fluid particle in three reference frames.

Fig. 2. A one-dimensional hydrodynamic component.

A code user only needs to specify $\mathbf{\Omega}$ and the point through which $\mathbf{\Omega}$ passes in the inertial frame of reference. This rotation matrix directly describes a three-dimensional rotation about an arbitrary axis. Once the component is rotated, the direction vector of the component is newly computed using the rotation matrix $\mathbf{R}$. Subsequently, the inclination and azimuthal angles are updated based on the new direction vector, and the two-phase flow pattern is also updated based on the new inclination angle.

It is well known that the conservation equations for thermodynamic properties, such as density, internal energy, and enthalpy, remain formally unchanged under a changing frame of reference, whereas the fictitious force terms appear in the momentum conservation equations. This also holds true for the two-fluid model [11]. The SPACE code uses the internal energy equations. Consequently, the effects of fictitious forces are only added to the momentum equations. The modified momentum equations for the gas, continuous liquid, and droplet fields in the SPACE code can be expressed as follows:

$$\alpha_g \rho_g \left(\frac{\partial u_g}{\partial t} + u_g \frac{\partial u_g}{\partial x} \right) = -\alpha_g \frac{\partial p}{\partial x} - F_{wg} u_g - F_{gl}(C_1 u_g - C_0 u_l)$$
$$- F_{gd}(u_g - u_d)$$
$$- \alpha_g \rho_g \left[\mathbf{g} + \ddot{\mathbf{R}} + \mathbf{\Omega} \times (\mathbf{\Omega} \times \mathbf{r}) + \dot{\mathbf{\Omega}} \times \mathbf{r} \right]_x \tag{2}$$

$$\alpha_l \rho_l \left(\frac{\partial u_l}{\partial t} + u_l \frac{\partial u_l}{\partial x} \right)$$
$$= -\alpha_l \frac{\partial p}{\partial x} - F_{wl} u_l - F_{gl}(C_0 u_l - C_1 u_g) - S_D(u_l - u_d)$$
$$- \alpha_l \rho_l \left[\mathbf{g} + \ddot{\mathbf{R}} + \mathbf{\Omega} \times (\mathbf{\Omega} \times \mathbf{r}) + \dot{\mathbf{\Omega}} \times \mathbf{r} \right]_x \tag{3}$$

$$\alpha_d \rho_d \left(\frac{\partial u_d}{\partial t} + u_d \frac{\partial u_d}{\partial x} \right)$$
$$= -\alpha_d \frac{\partial p}{\partial x} - F_{wd} u_d - F_{gd}(u_d - u_g) - S_E(u_d - u_l)$$
$$- \alpha_d \rho_d \left[\mathbf{g} + \ddot{\mathbf{R}} + \mathbf{\Omega} \times (\mathbf{\Omega} \times \mathbf{r}) + \dot{\mathbf{\Omega}} \times \mathbf{r} \right]_x \tag{4}$$

where α, ρ, u, p, $\mathbf{g}$, S_D, and S_E are the phase fraction, density, velocity, pressure, and gravity vector, droplet deposition rate, and droplet entrainment rate, respectively. The subscripts g, l, and d denote the gas, continuous liquid, and droplet phases, respectively. The operator $[\ldots]_x$ represents the projection of a force vector onto the one-dimensional direction of the corresponding hydrodynamic component. F_{wg}, F_{wl}, and F_{wd} are the wall friction coefficients for the gas, continuous liquid, and droplet fields, respectively. F_{gl} and F_{gd} are the interfacial friction coefficients between the gas and continuous liquid phases and the gas and droplet phases, respectively. C_1 and C_0 are coefficients related to the drift-flux interfacial friction model. The Coriolis force is not considered in Eqs. (2)–(4) because it is always normal to the one-dimensional flow direction.

In Eqs. (2)–(4), $\ddot{\mathbf{R}} = \ddot{R}_X \mathbf{I} + \ddot{R}_Y \mathbf{J} + \ddot{R}_X \mathbf{K}$ is the translational acceleration vector of the non-inertial reference frame relative to the inertial reference frame. The sum of the gravity and translational acceleration vectors is given by:

$$-\mathbf{g} + \ddot{\mathbf{R}} = \ddot{R}_X \mathbf{I} + \ddot{R}_Y \mathbf{J} + \left(9.81 + \ddot{R}_Z \right) \mathbf{K} \tag{5}$$

Next, $\mathbf{\Omega} \times (\mathbf{\Omega} \times \mathbf{r})$ and $\dot{\mathbf{\Omega}} \times \mathbf{r}$ account for the centrifugal and Euler forces, respectively, where $\mathbf{\Omega} = \Omega_x \mathbf{i} + \Omega_y \mathbf{j} + \Omega_z \mathbf{k}$, $\dot{\mathbf{\Omega}} = \dot{\Omega}_x \mathbf{i} + \dot{\Omega}_y \mathbf{j} + \dot{\Omega}_z \mathbf{k}$, and $\mathbf{r} = r_x \mathbf{i} + r_y \mathbf{j} + r_z \mathbf{k}$ are vectors in the non-inertial frame.

The centrifugal and Euler forces are calculated as

$$\mathbf{\Omega} \times (\mathbf{\Omega} \times \mathbf{r}) = \left[\Omega_y (\Omega_x r_y - \Omega_y r_x) - \Omega_z (-\Omega_x r_z + \Omega_z r_x) \right] \mathbf{i}$$
$$+ \left[-\Omega_x (\Omega_x r_y - \Omega_y r_x) + \Omega_z (\Omega_y r_z - \Omega_z r_y) \right] \mathbf{j}$$
$$+ \left[\Omega_x (-\Omega_x r_z + \Omega_z r_x) - \Omega_y (\Omega_y r_z - \Omega_z r_y) \right] \mathbf{k} \tag{6}$$

$$\dot{\mathbf{\Omega}} \times \mathbf{r} = \left(-r_y \dot{\Omega}_z + r_z \dot{\Omega}_y \right) \mathbf{i} + \left(r_x \dot{\Omega}_z - r_z \dot{\Omega}_x \right) \mathbf{j}$$
$$+ \left(-r_x \dot{\Omega}_y + r_y \dot{\Omega}_x \right) \mathbf{k} \tag{7}$$

In the SPACE code, the absolute position of each local component is not updated, but only its direction vector is updated. Because the absolute local positions remain unchanged, we can take $\Omega_x = \Omega_X$, $\Omega_y = \Omega_Y$, and $\Omega_z = \Omega_Z$. However, because each component is actually rotated, the total sum of the acceleration vectors ($-\mathbf{g} + \ddot{\mathbf{R}} + \mathbf{\Omega} \times (\mathbf{\Omega} \times \mathbf{r}) + \dot{\mathbf{\Omega}} \times \mathbf{r}$) is also rotated through the rotation matrix $\mathbf{R}$. Finally, the total acceleration vector acting on each local hydrodynamic component is projected onto the one-dimensional direction of the component in the non-inertial reference frame.

3. Results and discussion

3.1. Tests in two-dimensional pipeline loops

To verify the general dynamic motion model, code calculations were performed on the conceptual problems for two-dimensional and three-dimensional pipe loops. Fig. 3 shows the square manometer that is arranged in the XZ-plane. The manometer comprises 4 identical pipes, each of which has a length $L = 1$ m and a diameter $d = 0.007854$ m. Initially, the 2 vertical pipes were half full of saturated water at 100 bar.

Fig. 4 shows the result when the monometer oscillates with an amplitude of $30°$ and a period of 40 s. The oscillation axis is the line $(X, Y, Z) = (0.5$ m, 0 m, 0.5 m$)$ in the inertial frame of reference, which passes through the center point of the manometer arrangement. In the figure, water length refers to the length the water fills each pipe. As shown, the water lengths over time are in good agreement with the theoretical predictions.

Fig. 5 shows the results when the manometer is rotated continuously. Each pipe becomes empty and filled repeatedly as the manometer continues to rotate. The counterclockwise and clockwise rotations show the same results, except for the fill and drain directions. Because the rotation speed considered is not large, the
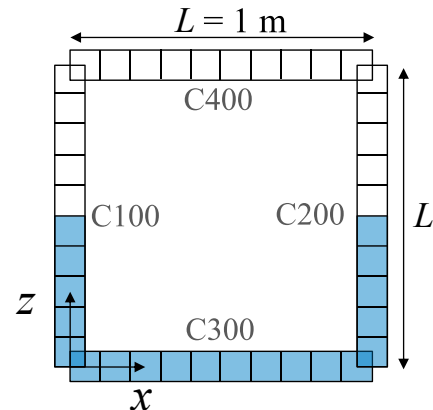

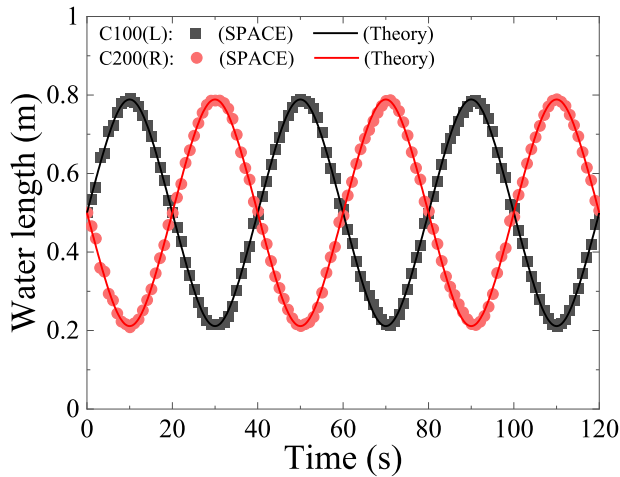**Fig. 3.** Square manometer—initially half full of saturated water.

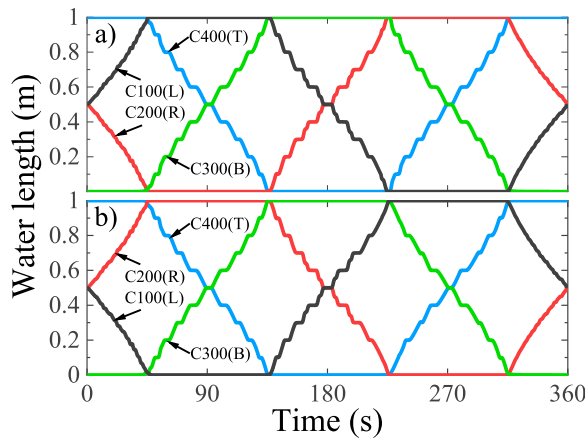**Fig. 4.** Results when the manometer oscillates with an amplitude 30° and a period 40 s.

Fig. 5. Results when the monometer is continuously rotated at (a) counterclockwise 1°/s rotation and (b) clockwise 1°/s.

Fig. 6. Three cases to test the centrifugal effect.

Fig. 7. Results when the manometer is rotated about the z-axis: (a) Ω increases linearly to 90°/s for the first 40 s, and then remains at 90°/s, (b) Ω increases linearly to 360°/s at 40 s and is maintained at 360°/s after 40 s.

rotational acceleration effects are insignificant. The motions of water in the pipes were affected mainly by changes in the direction of gravity due to rotation.

Next, we consider the cases in which the centrifugal and/or Euler forces appear. Fig. 6 shows three cases where the manometer is rotated about the z-axis. In Fig. 6(a), the angular velocity Ω is not so high that the water level is slightly higher in the right pipe (C200) than in the left pipe (C100). In Fig. 6(b), the angular velocity is high enough to push the water radially in the bottom pipe so that the left pipe empties completely and the top pipe is partially filled. L' and $L - L'$ represents the water lengths in the bottom and top pipes, respectively. In Fig. 6(c), the manometer is horizontally accelerated at $\ddot{R}_X$ and is simultaneously rotated about the z-axis.

Fig. 7 shows the results when the manometer is rotated about the z-axis. In Fig. 7(a), Ω increases linearly to 90°/s for the first 40 s, and then remains at 90°/s. The final distribution of water in the rotating frame is shown in Fig. 6(a), where Δh is theoretically calculated as $\Omega^2 L^2/(4g) = 0.0628$ m. In Fig. 7(a), the dashed lines indicate the theoretical water levels $L/2 + \Omega^2 L^2/(4g)$ and $L/2 - \Omega^2 L^2/(4g)$, respectively. As shown, the water levels in the left and right pipes agree well with the theoretical predictions. Fig. 7(b) shows the results when Ω increases linearly to 360°/s for the first

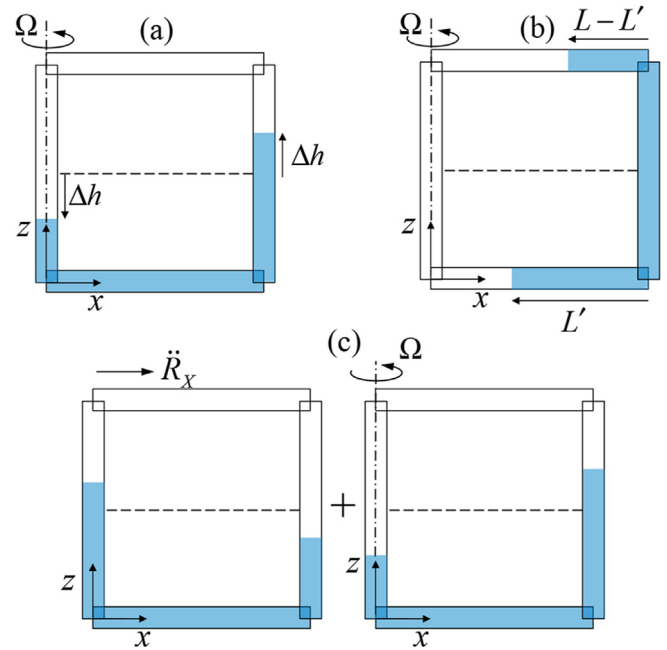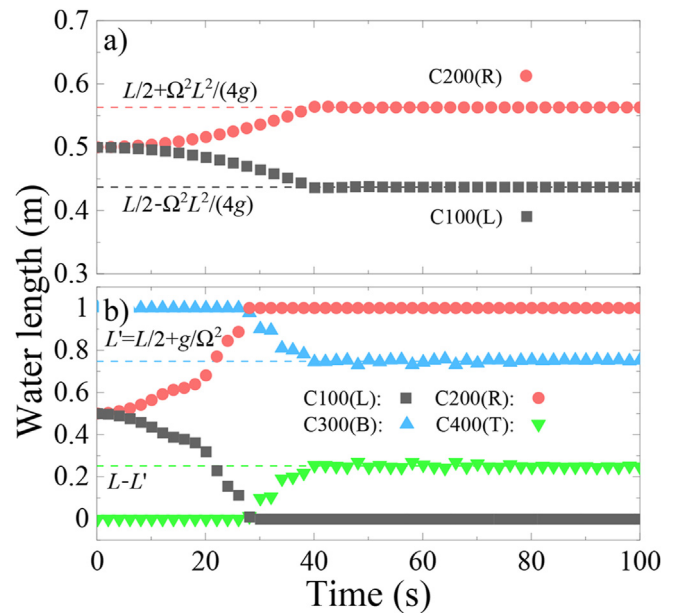40 s, and then remains at 360°/s. The final distribution of water in the rotating frame eventually is shown in Fig. 6(b), where L' is theoretically calculated as $L/2 + g/\Omega^2 = 0.748$ m. In Fig. 7(b), the dashed lines indicate the theoretical water lengths L' and $L - L'$, respectively. As shown, the water lengths in the bottom and top pipes agree well with the theoretical predictions.

Fig. 8 shows the results when the manometer is rotated and simultaneously horizontally accelerated. In Fig. 8(a), $\ddot{R}_X$ increases linearly to 2 m/s² for the first 40 s and then is maintained at 2 m/s². From 80 s, Ω increases linearly to 15°/s for the next 40 s and then remains at 15°/s. After 80 s, the water column oscillates between
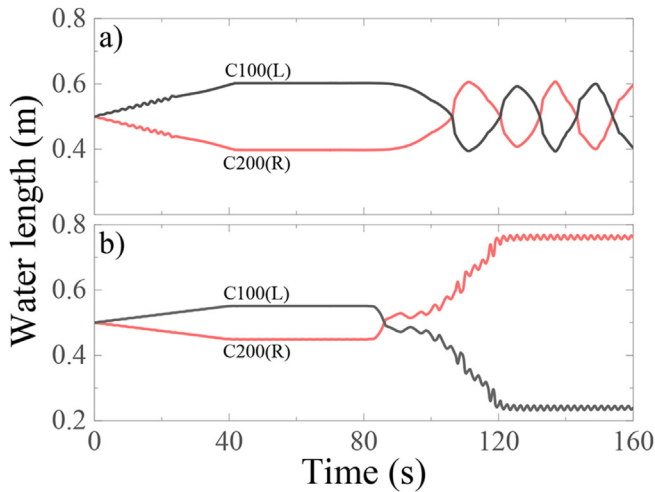
**Fig. 8.** Results: (a) $\ddot{R}_X$ increases linearly to 2 m/s^2 for the first 40 s, and then is maintained at 2 m/s^2. From 80 s, Ω increases linearly to 15°/s for the next 40 s, and then remains at 15°/s, (b) $\ddot{R}_X$ increases linearly to 1 m/s^2 for the first 40 s, and then is maintained at 1 m/s^2. From 80 s, Ω increases linearly to 180°/s for the next 40 s, and then remains at 180°/s.

the left and right pipes as the positions of the left pipe (C100) and the right pipe (C200) are periodically exchanged while the manometer is horizontally accelerated. Because Ω is not high, the centrifugal effect is smaller than the horizontal acceleration effect. By contrast, in Fig. 8(b), $\ddot{R}_X$ increases linearly to 1 m/s^2 for the first 40 s, and is then maintained at 1 m/s^2. From 80 s, Ω increases linearly to 180°/s for the next 40 s and then remains at 180°/s. As shown in Fig. 8(b), after 100 s, the centrifugal effect becomes greater than the horizontal acceleration effect. After 120 s, the centrifugal effect is dominant so that the water level is higher in the right pipe than in the left pipe. Each time the manometer turns 180°, the horizontal acceleration effect is reversed. However, because the effect of the horizontal acceleration is small, though there are some oscillations after 120 s, the water levels do not change significantly.

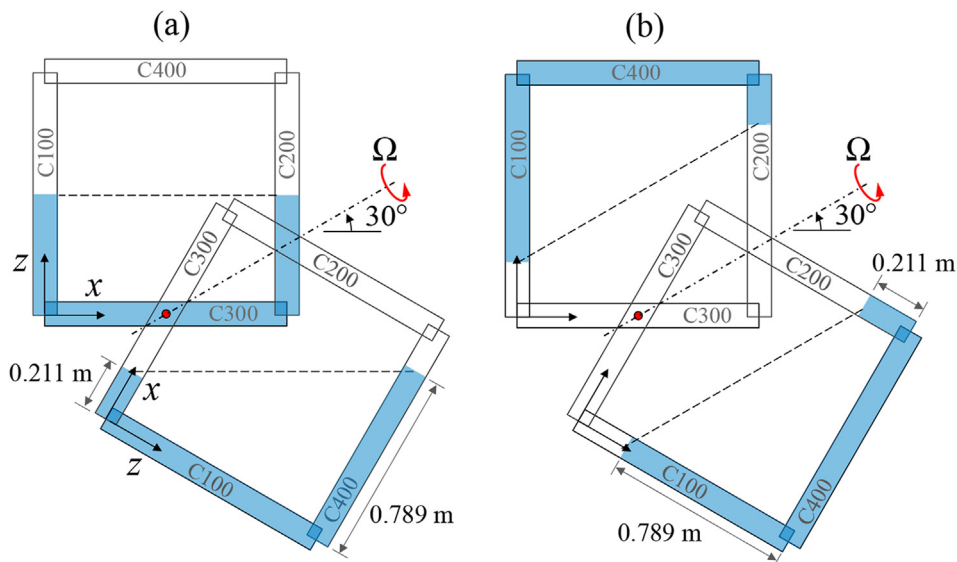In the above three rotation cases, the rotation axes were parallel
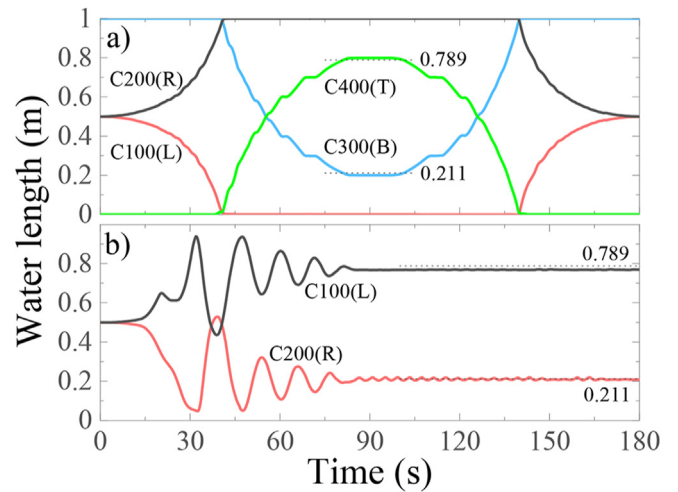
Fig. 10. Results: (a) $\Omega = 2$°/s, (b) $\ddot{R}_Z = -9.81$ m/s^2 and $\Omega = 90$°/s.
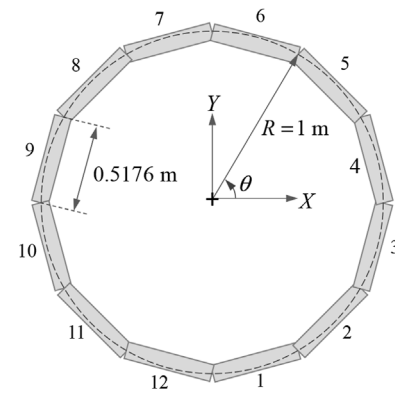
Fig. 11. Torus model to test the Euler force effect.

to the Z-axis of the inertial frame of reference. To test the rotation about an arbitrary axis, the rotation axis was assumed to be tilted in the inertial frame of reference. Fig. 9 shows the two cases in which

Fig. 9. Square manometer: (a) $\Omega = 2$°/s, (b) $\ddot{R}_Z = -9.81$ m/s^2 and = 90°/s.

the rotation axes pass through the point $(X, Y, Z) = (0.5 \text{ m}, 0 \text{ m}, 0 \text{ m})$ and are tilted 30° from the X-axis. In Fig. 9(a), the rotation speed is very small ($\Omega = 2°/s$) so that the motion of water is affected mainly by changes in the direction of gravity due to rotation. In Fig. 9(b), the manometer falls freely while rotating at a relatively large speed of $\Omega = 90°/s$. In this case, because the gravity effect disappears, the final water distribution is determined only by the Centrifugal force. Fig. 10(a) shows the code calculation result for the case shown in Fig. 9(a). The values of 0.789 m and 0.211 m are the theoretically predicted water lengths when the connection part between the top pipe (C400) and the left pipe (C100) reaches its lowest location. Fig. 10(b) shows the result when Ω increases linearly to 90°/s for the first 100 s and then remains at 90°/s. The final water lengths agree well with the theoretical predictions. The good agreement demonstrates that the three-dimensional rotation about an arbitrary axis was well implemented.

We now turn to the Euler force effect. Fig. 11 shows a nodding diagram for a horizontal torus consisting of 12 identical cells. Each cell has a length of 0.5176 m and a diameter of 0.1 m. This configuration is to model a circular torus with a radius of $R = 1$ m. The torus is assumed to oscillate along the z-axis. The counterclockwise rotation angle is set to $\theta = A_0[1 - \cos(\omega t)]$. Then, the angular velocity and angular acceleration are calculated as $\Omega = A_0\omega \sin(\omega t)$ and $\dot{\Omega} = A_0\omega^2 \cos(\omega t)$, respectively. Initially, the torus was under the 100-bar saturation with $\alpha_g = 0.5$, $\alpha_l = 0.45$, and $\alpha_d = 0.05$. The wall friction, droplet deposition, and droplet entrainment models were not to be computed.

We will obtain the theoretical solutions for u_l and u_d in the complete circular torus. The spatial derivative terms in Eqs. (3) and (4) can be deleted in consideration of the closed loop of the torus. Because the wall friction is not computed, the circumferential oscillation of the torus does not affect the vapor and water velocities. Therefore, the water and droplet remain motionless in the fixed frame. Neglecting the gravity, wall fraction, interfacial friction, droplet entrainment, droplet deposition terms and setting $\ddot{\mathbf{R}}$ and $\boldsymbol{\Omega} \times (\boldsymbol{\Omega} \times \mathbf{r})$ to zero, Eqs. (3) and (4) can be simplified as $du_l/dt = -\dot{\Omega}R = -A_0\omega^2 \cos(\omega t)R$ and $du_d/dt = -A_0\omega^2 \cos(\omega t)R$, respectively. Subsequently, we obtain $u_l = u_d = -A_0\omega R \sin(\omega t)$. Because the fluids inside the torus remains motionless in the fixed frame, each fluid velocity measured in the moving frame is the negative of the torus velocity $u_{\text{torus}} = \Omega R = A_0\omega R \sin(\omega t)$.

Fig. 12 compares the SPACE results with the theoretical results when $A_0 = 30° = \pi/6$ and $T = 2\pi/\omega = 10$ s. As expected, the predicted water and droplet velocities are nearly the same. Theory

Fig. 12. Water velocity measured in the moving torus.

indicates $u = -A_0\omega R \sin(\omega t)$. The predicted amplitudes are slightly smaller than theoretical amplitude ($A_0\omega R$). This underprediction is attributed to the fact that the modeled torus is not circular, as shown in Fig. 11. In the SPACE code, the length of one momentum cell is set to be the distance between the centers of two adjacent cells. With reference to Fig. 11, the length of one momentum cell is calculated to be 0.5 m. Meanwhile, the circumferential length of one segment of the circular torus, which corresponds to 30°, is calculated to be 0.524 m. Therefore, the SPACE code, which is based on the finite-volume method, calculated the Euler effect to be 0.5/0.524 = 0.954 times smaller than the theoretical solution. Furthermore, the distance between the momentum cell center and the rotation axis is computed as 0.933 m. Thus, when calculating the Euler force, R was set to be 0.933 m instead of 1.0 m, which leads to a decrease in the Euler force by 6.7%. Overall, the Euler force was calculated to be $0.954 \times 0.933 = 0.890$ times smaller than the theoretical solution. In Fig. 12, Modified theory indicates the solution corrected by a factor of 0.890. The excellent agreement between the predicted velocities and Modified theory means that the fictitious force terms in the momentum equations work as designed.

3.2. Tests in three-dimensional pipeline loops

So far, one-dimensional flows in two-dimensional pipeline loos have been discussed. As mentioned before, since the motion of an ocean nuclear reactor can be three-dimensional, the reactor must be modeled in the three-dimension space. In this respect, it is necessary to check the prediction ability for one-dimensional flows in a three-dimensional pipeline loop. Fig. 13 shows a schematic diagram of the three-dimensional pipeline loop considered in this study. The loop diameter is 0.1 m and is partially filled with water at a saturation pressure of 10 bar. The rotation axis passes through the point (0.25 m, −0.5 m, 0 m).

In the first test, the pipeline was set to rotate at $\Omega = -2°/s$ about the axis with $\theta = 45°$ and $\varphi = 30°$. The rotation speed is so small that the motion of water is determined mainly by changes in the direction of gravity due to rotation. In the second test, the pipeline was set to fall freely while rotating at $\Omega = -90°/s$ about the axis with $\theta = 30°$ and $\varphi = 75°$. In this condition, because the gravity effect disappeared, the final water distribution was determined only by the Centrifugal force. To validate the code calculation results, we also performed multi-dimensional CFD simulations based on the approach suggested by Ref. [11], using the ANSYS Fluent solver [15]. Fig. 14 shows the CFD results for the first and second test conditions, respectively. In Fig. 14(a), the right figure shows the initial water distribution and the left figure shows the water distribution when the initial loop is clockwise rotated by 240°. In Fig. 14(b), the left and right figures show the water distributions when the loops have made 15.5 and 16 rotations, respectively. It is seen that the flow nearly reaches a steady state.

Fig. 15 shows the changes in the water lengths of C200 and C500 during the first two rotations of the loop according to the first test condition. In the SPACE calculation, the pipeline was modeled with a total of 51 cells. Overall, the SPACE results agree well with the CFD results. For both the SPACE code and CFD, the difference between two water lengths becomes the smallest at about 120 s and 300 s. As a side note, the left loop shown in Fig. 14(a) corresponds to time 120 s. The slight differences between the SPACE and CFD results at 120 s and 300 s may be due to the pipeline modeling. The volume of each connecting part between adjacent straight pipes is not considered in the SPACE modeling, whereas it is considered in the CFD modeling, as shown in Fig. 14.

Fig. 16 shows the changes in the water lengths of C200 and C500 during the first fifty rotations of the loop according to the second
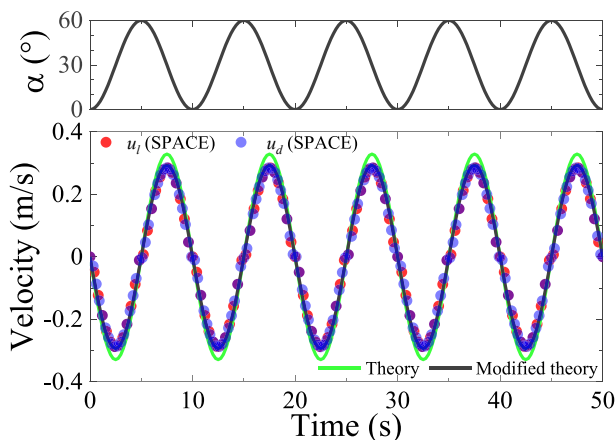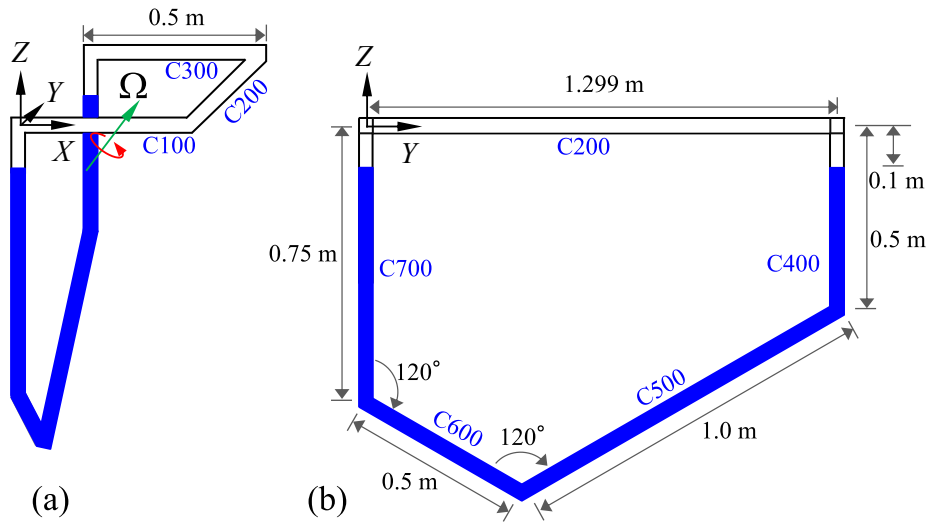
Fig. 13. Initial water distribution in the three-dimensional pipeline loop: (a) Isometric view, (b) YZ-plane view.

Fig. 15. Result for $\Omega = -2°/s$ about the axis with $\theta = 45°$ and $\varphi = 30°$.

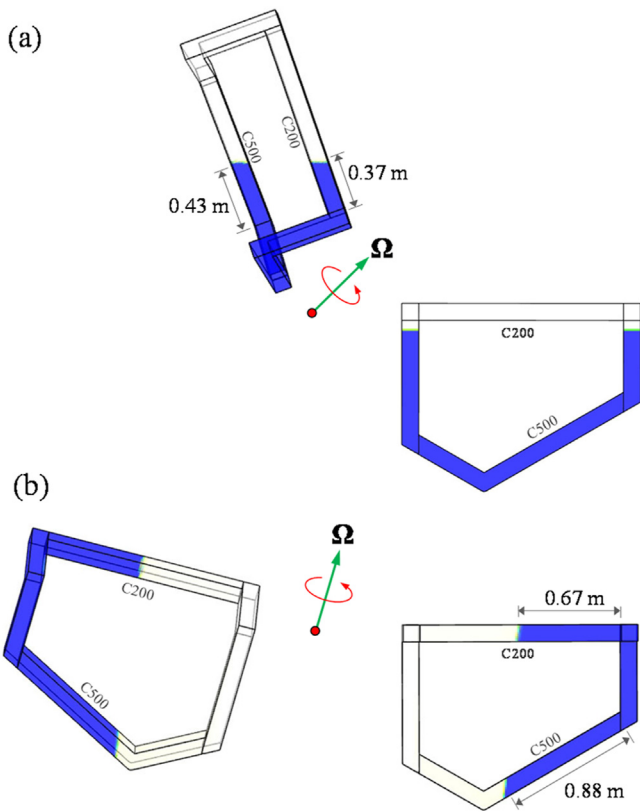**Fig. 14.** CFD results (View toward the YZ-plane): (a) $\Omega = -2°/s$ about the axis with $\theta = 45°$ and $\varphi = 30°$, (b) $\ddot{R}_Z = -9.81$ m/s² and $\Omega = -90°/s$ about the axis with $\theta = 30°$ and $\varphi = 75°$.
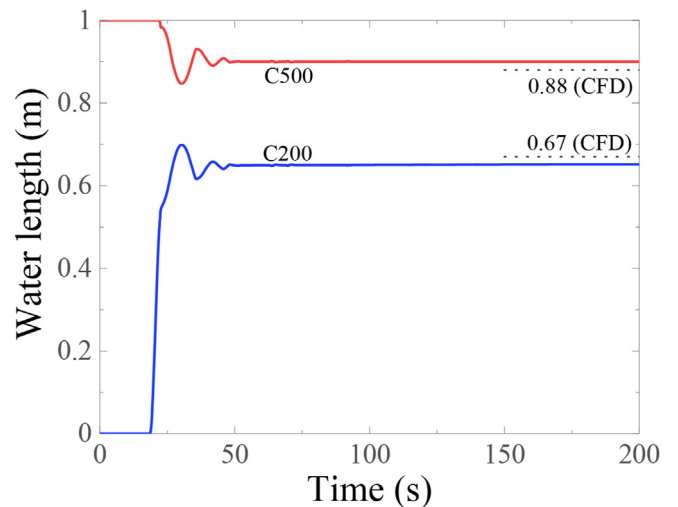
Fig. 16. Result for $\ddot{R}_Z = -9.81$ m/s² and $\Omega = -90°/s$ about the axis with $\theta = 30°$ and $\varphi = 75°$.

test condition. The values of 0.88 and 0.67 correspond to the water lengths shown in Fig. 14(b), where the loop has made 16 rotations. It is seen in Fig. 16 that the final water lengths are close to the CFD predictions. The slight differences from the CFD predictions are attributed to the fact that though the water distribution nearly reached a steady state after 16 rotations in the CFD, the water lengths were still converging with very small amplitudes. In addition, a small number of cells in the SPACE code calculation may be
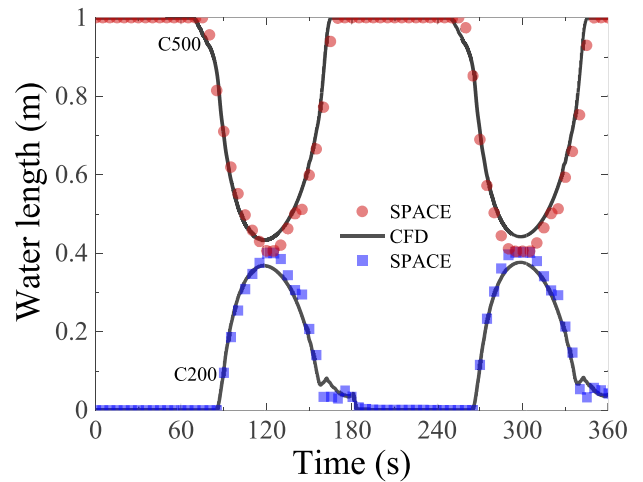
one of reasons.

4. Conclusions

We have presented recent efforts to incorporate a dynamic motion model into the SPACE code. A rotation system that describes three-dimensional rotations about an arbitrary axis was implemented, and modifications were made to the one-dimensional momentum equations to reflect the linear and rotational acceleration effects.

Various conceptual problems were tested to demonstrate the code capability to solve a problem utilizing a rotational frame of reference. When the rotation speed was small or the oscillation period large, the motion of water in the manometer was governed by changes in the direction of gravity rather than by rotational acceleration effects. The code calculation results agreed well with the theoretical predictions. For both moderate and large rotation speeds at which the Centrifugal and/or Euler forces appear, the code calculation results showed excellent agreement with the theoretical predictions.

In addition, verification tests were conducted for rotations about arbitrarily tilted axes. The code results for the two-dimensional manometer with a tilted rotation axis showed good agreement with theoretical predictions. The code results for the three-dimensional pipeline loop with a tilted rotation axis also agreed well with the multi-dimensional CFD results. These excellent results mean that the SPACE code has the prediction ability for one-dimensional flows in a three-dimensional loop under rotations about an arbitrary axis.

This study focuses the three-dimensional dynamic motion model rather than physical model. In the future, multi-dimensional simulation capabilities will be implemented, and the code will be validated using available experimental data. The SPACE code is expected to contribute to the design of ocean nuclear power plants.

Declaration of competing interest

The authors declare that they have no known competing financial interests or personal relationships that could have appeared to influence the work reported in this paper.

References

[1] J. Buongiorno, J. Jurewicz, M. Golay, N. Todreas, The offshore floating nuclear plant concept, Nucl. Technol. 194 (2016) 1–14.
[2] K. Lee, K.-H. Lee, J.I. Lee, Y.H. Jeong, P.-S. Lee, A new design concept for offshore nuclear power plants with enhanced safety features, Nucl. Eng. Des. 254 (2013) 129–141.
[3] Y.K. Panov, V.I. Polunichev, K.V. Zverev, Nuclear Floating Power Desalination Complexes, 1998. IAEA-TECDOC–1056.
[4] K. Shirvan, R. Ballinger, J. Buongiorno, C. Forsberg, M. Kazimi, N. Todreas, Technology selection for offshore underwater small modular reactors, Nucl. Eng.Technol. 48 (2016) 1303–1314.
[5] I. Ishida, T. Kusunoki, H. Murata, T. Yokomura, M. Kobayashi, H. Nariai, Thermal-hydraulic behavior of a marine reactor during oscillations, Nucl. Eng. Des. 120 (1990) 213–225.
[6] T. Ishida, T. Kusunoki, M. Ochiai, T. Yao, K. Inoue, Effects by sea wave on thermal-hydraulics of marine reactor system, J. Nucl. Sci. Technol. 32 (1995) 740–751.
[7] J.H. Kim, G.C. Park, Development of Retran-03/mov code for thermal-hydraulic analysis of nuclear reactor under moving conditions, Journal of the Korean Nuclear Society 28 (1996) 542–550.
[8] H.-K. Beom, G.-W. Kim, G.-C. Park, H.K. Cho, Verification and improvement of dynamic motion model in mars for marine reactor thermal-hydraulic analysis under ocean condition, Nucl. Eng.Technol. 51 (2019) 1231–1240.
[9] G.L. Mesina, D.L. Aumiller, F.X. Buschman, M.R. Kyle, Modeling moving systems with Relap5-3d, Nucl. Sci. Eng. 182 (2016) 83–95.
[10] B.H. Yan, L. Yu, The development and validation of a thermal hydraulic code in rolling motion, Ann. Nucl. Energy 38 (2011) 1728–1736.
[11] B.J. Kim, M.H. Kim, S.W. Lee, K.D. Kim, Two-fluid equations for two-phase flows in moving systems, Nucl. Eng.Technol. 51 (2019) 1504–1513.
[12] https://en.wikipedia.org/wiki/Euler_angles..
[13] S.J. Ha, C.E. Park, K.D. Kim, C.H. Ban, Development of the space code for nuclear power plants, Nucl. Eng.Technol. 43 (2011) 45–62.
[14] https://en.wikipedia.org/wiki/Rotation_matrix..
[15] ANSYS, Ansys Fluent Theory Guide, Release 19.2, 2018.